#### Research Article

Chao Feng, Kai Dong, Rong Zhu\*, Tao Lin, Jian-feng Dong, Tao Xia, and Xin Ren

# Effect of ambient temperature on the jet characteristics of a swirl oxygen lance with mixed injection of $CO_2 + O_2$

https://doi.org/10.1515/htmp-2022-0239 received June 10, 2022; accepted August 26, 2022

**Abstract:** O<sub>2</sub> mixed with CO<sub>2</sub> gas has been successfully applied in converter smelting; however, up to now, there have been few studies regarding the jet characteristics of the mixed injection of the swirl oxygen lance nozzle and the influence of different ambient temperature conditions on jet characteristics compared with common nozzles. In this study. Fluent software was used to simulate the jet characteristics of a four-hole common nozzle and a fourhole swirl nozzle under four different ambient temperature conditions to inject 95%  $O_2$  + 5%  $CO_2$  and analyze the influence of different ambient temperatures on nozzle-jet characteristics. The results show that with an increase in the ambient temperature, the jet-axis velocity and nozzle centerline speed increase. Under the same distance condition, the distance between the maximum radial velocity point of the jet and the centerline of the nozzle becomes larger, with a velocity greater than that of the swirl nozzle. However, the influence of the ambient temperature on the offset of the jet centerline is small. With an increase in the ambient temperature and distance, the

\* Corresponding author: Rong Zhu, School of Metallurgical and Ecological Engineering, University of Science and Technology Beijing, Beijing 100083, China; Beijing Key Laboratory of Research Center of Special Melting and Preparation of High-End Metal Materials, University of Science and Technology Beijing, Beijing 100083, China, e-mail: zhurong1\_1201@126.com

Chao Feng, Kai Dong: School of Metallurgical and Ecological Engineering, University of Science and Technology Beijing, Beijing 100083, China; Beijing Key Laboratory of Research Center of Special Melting and Preparation of High-End Metal Materials, University of Science and Technology Beijing, Beijing 100083, China Tao Lin: School of Metallurgical and Ecological Engineering, University of Science and Technology Beijing, Beijing 100083,

China; Jiangsu Province Binxin Steel Group Co., Ltd, Jiangsu 222000, China

Jian-feng Dong, Tao Xia, Xin Ren: School of Metallurgical and Ecological Engineering, University of Science and Technology Beijing, Beijing 100083, China

jet-axis temperature increases and the temperature of the nozzle centerline decreases. The research results can provide a theoretical reference for the optimal design of a  $CO_2 + O_2$  swirl oxygen lance nozzle.

Keywords: swirl nozzle, jet, ambient temperature, velocity, temperature distribution

#### 1 Introduction

Converter steelmaking is an important aspect of the long smelting process, and an oxygen lance is a critical tool in converter smelting. The jet characteristics of the oxygen lance nozzle directly affect slag-making and the removal of harmful elements in the smelting process. The top oxygen jet contains the oxygen and stirring energy required for converter smelting, which plays an important role in metallurgical reactions, smelting process stability, and smelting rhythm in the converter. Therefore, studying the jet characteristics of an oxygen lance nozzle is of great significance [1–8].

Many studies and analyses of the jet characteristics of the traditional oxygen lance nozzle and swirl oxygen lance nozzle for top-blowing oxygen have been performed through numerical simulations and experiments [9–14]. Li and Cang [15] conducted research into the behavior of a low-temperature supersonic oxygen jet in a high-temperature environment using four two-equation turbulence models: the standard  $\kappa$ – $\varepsilon$  model, realizable  $\kappa$ - $\varepsilon$  model, standard  $\kappa$ - $\omega$  model, and shear stress transport  $\kappa$ - $\omega$  model. The results show that with an increase in the ambient temperature, the axial velocity of the jet decreases and the length of the jet potential core increases. Liu et al. [16] conducted cold-state experiments on the two-parameter oxygen lance nozzle, and the results showed that the small orifice and large orifice had different effects on the stirring of the molten pool. Wei et al. [17] studied the effect of gas temperature on the characteristics of a supersonic jet, and the results showed

that the potential core length of a supersonic jet increases with the increase in temperature. He et al. [18] studied the effect of a supersonic oxygen jet on molten steel and slag. The results showed that with the increase in spray gun height, the maximum velocity at 0.2 m below the liquid steel surface decreased. Lv et al. [19] studied the stirring effect of different oxygen lance nozzles on the molten pool. The results show that when the swirl oxygen lance is used, the constant velocity zone in the molten pool is large. Li et al. [20] carried out a numerical simulation of the supersonic jet of a nozzle-twisted spray gun. The results show that the enhanced vortex weakens the coalescence of the jet and accelerates the attenuation of the axial velocity. Yang et al. [21] studied the effect of temperature on the performance of rotating supersonic jets. The results show that preheating oxygen improves the jet center velocity and enhances the velocity fluctuation.

There have been many studies on improving the jet characteristics of the traditional oxygen lance nozzle and swirl nozzle [22,23], mainly including changing the position and parameters of the nozzle. CO<sub>2</sub> can produce some beneficial effects in converter smelting [24–29]. However, less attention has been given to the jet characteristics of the swirling oxygen lance nozzle at room temperature (300 K) [30], early smelting stage (1,573 K), middle smelting stage (1,773 K), and late smelting stage (1,973 K) for a combination of  $CO_2$  and mixed injection of  $O_2 + CO_2$ . In this study, CFD software was used to simulate the performance of the common oxygen lance nozzle and swirl oxygen lance injection at different ambient temperatures. This analysis of the jet characteristics of the swirl oxygen lance nozzle and the common oxygen lance nozzle provides theoretical support for the design and use of a swirl oxygen lance nozzle.

## 2 Mathematical model

### 2.1 Application of the equation

In order to meet the accuracy requirements of the simulation process, the following assumptions are proposed:

- (1) Gas is a Newtonian fluid with constant specific heat in a compressible ideal state.
- (2) The gas flow in the Laval nozzle is a compressible non-isothermal process.
- (3) Ignoring the friction resistance, it is considered that the inner wall of the nozzle is smooth.

According to the assumptions, the equations used in this study are as follows [21,28]:

(1) The mass, momentum, and energy equations are expressed as follows:

$$\frac{\partial(\rho u_i)}{\partial x_i} = 0,\tag{1}$$

$$\frac{\partial(\rho u_i u_j)}{\partial x_i} = -\frac{\partial p}{\partial x_i} + \frac{\partial(\tau_{ij} - \rho \overline{u_i} \overline{u_j})}{\partial x_j},\tag{2}$$

$$\frac{\partial}{\partial t}(\rho E) + \nabla \cdot (\overrightarrow{v}(\rho E + \rho))$$

$$= \nabla (k_{\text{eff}} \nabla T - \sum_{i} h_{i} \overrightarrow{J_{i}} + (\overrightarrow{\tau_{\text{eff}}} \cdot \overrightarrow{v})) + S_{\text{h}},$$
(3)

where  $\rho$  is the density of gas, kg·m<sup>-3</sup>,  $u_i$  and  $u_j$  are the ith and jth direction's velocity, m·s<sup>-1</sup>;  $\tau_{ij}$  is the viscous stress, Pa;  $\overrightarrow{v}$  is the instantaneous velocity of the fluid, m·s<sup>-1</sup>; t is the time, s;  $\overrightarrow{J_i}$  was the diffusion flux of species i;  $k_{\rm eff}$  is the effective thermal conductivity, W·(m<sup>-2</sup>·K<sup>-1</sup>).

$$\tau_{ij} = \mu \left( \frac{\partial u_j}{\partial x_i} + \frac{\partial u_i}{\partial x_j} - \frac{2\partial u_k}{3\partial x_k} \delta_{ij} \right). \tag{4}$$

 $\boldsymbol{\mu}$  is Sutherland's viscosity, and the equation is as follows:

$$\mu = 2.67 \times 10^{-6} \left(\frac{C_E}{C_l^2}\right) \sqrt{\frac{M}{T}},$$
 (5)

where  $\delta_{ij}$  is the Kronecker delta, if i=j, therefore  $\delta_{ij}=0$ , if  $i\neq j$ , therefore  $\delta_{ij}=1$ ;  $\mu$  is molecular viscosity (Pa·s<sup>-1</sup>); M is molecular weight (kg·kmol<sup>-1</sup>), M=32.6 kg·kmol<sup>-1</sup>; T is exit boundary temperature (K).  $C_{\rm E}$  is Lennard–Jones energy parameter (K) and  $C_{\rm E}=195.2$  K.  $C_{\rm I}$  is Lennard–Jones characteristic length (Å) and  $C_{\rm I}=3.941$  Å;  $c_{\rm p}$  is the specific heat capacity, J·(kg<sup>-1</sup>·K<sup>-1</sup>);  $q_i$  is the heat conduction vector.

$$q_j = -k_T \frac{\partial T}{\partial x_i},\tag{6}$$

where  $k_{\rm T}$  is the thermal conductivity coefficient (W·m<sup>-1</sup>·K<sup>-1</sup>).

The turbulence kinetic energy k and dissipation rate  $\varepsilon$  equation of the standard  $k-\varepsilon$  model are as follows:

$$\frac{\partial}{\partial t}(\rho k) + \frac{\partial}{\partial x_i}(\rho k v_i) = \frac{\partial}{\partial x_j} \left[ \left( \mu + \frac{\mu_t}{\mu_k} \right) \frac{\partial k}{\partial x_j} \right] + G_k + G_b - \rho \varepsilon - Y_M + S_k,$$
 (7)

$$\frac{\partial}{\partial t}(\rho \varepsilon) + \frac{\partial}{\partial x_{i}}(\rho \varepsilon v_{i}) = \frac{\partial}{\partial x_{j}} \left[ \left( \mu + \frac{\mu_{t}}{\mu_{\varepsilon}} \right) \frac{\partial \varepsilon}{\partial x_{i}} \right] + C_{1\varepsilon} \frac{\varepsilon}{k} (G_{k} + C_{3\varepsilon} G_{b}) - C_{2\varepsilon} \rho \frac{\varepsilon^{2}}{k} + S_{\varepsilon},$$
(8)

$$\mu_t = \rho C_\mu \frac{k^2}{\varepsilon^2},\tag{9}$$

where  $G_k$  is the turbulence energy generated by laminar velocity gradient (J);  $G_b$  is the turbulence energy generated by buoyancy;  $Y_M$  is the fluctuation due to excessive diffusion of compressible turbulence (J);  $v_i$  is the velocity of the fluid in the ith direction, m·s<sup>-1</sup>;  $\sigma_k$  and  $\sigma_{\varepsilon}$  are turbulent Prandtl numbers for k equation and  $\varepsilon$  equation;  $\sigma_k = 1.0$  and  $\sigma_{\varepsilon} = 1.3$ ;  $C_{1\varepsilon}$ ,  $C_{2\varepsilon}$ , and  $C_{3\varepsilon}$  are constants equal to 1.44, 1.92, and 0.8, respectively;  $\mu_t$  is the turbulent viscosity; and  $C\mu = 0.09$ .

#### 2.2 Calculation of the condition setting

Considering the interaction between multi-jets, in order to simulate the real state of the jet more accurately, the mesh model of the oxygen lance of the four-hole full-scale Laval nozzle was established by using ICEM CFD software. This article mainly studies the jet characteristics of common and swirl oxygen lance nozzles. Detailed parameters are shown in Table 1. The outer diameter of the oxygen lance nozzle is 273 mm, and the molten pool depth of the 120 t converter is 1,310 mm. In the actual smelting process, the height of the oxygen lance nozzle

Table 1: Main technical parameters

Parameters	Common nozzle	Swirling flow nozzle
Number of holes	4	4
Mach number	2.02	2.02
$Dt_1 (mm)$	38.2	38.2
$De_1 (mm)$	50.1	50.1
$\alpha_1$ (°)	13	13
$\alpha_2$ (°)	3.5	3.5
$\alpha_3$ (°)	0	10
Flow (Nm <sup>3</sup> ·h <sup>-1</sup> )	24,000	24,000
Gas medium	$95\% \ O_2 + 5\% \ CO_2$	95% O <sub>2</sub> + 5% CO <sub>2</sub>

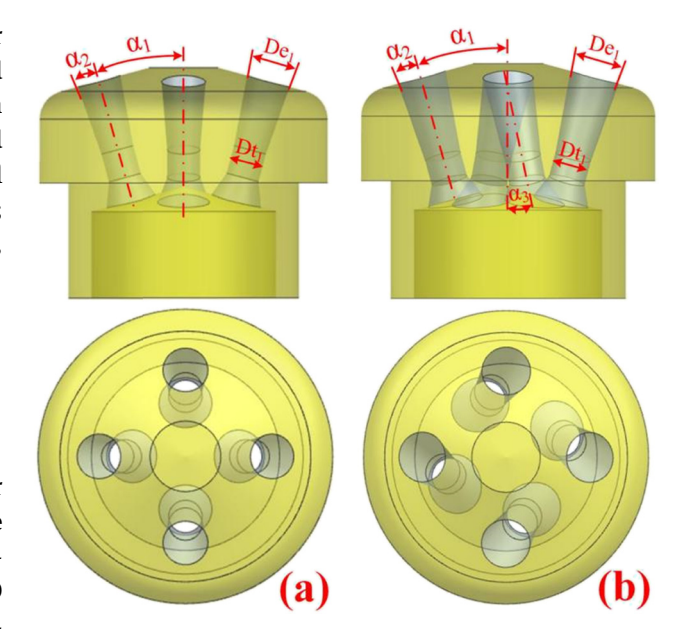


Figure 1: Nozzle shapes of (a) four-hole common nozzle and (b) four-hole swirl nozzle.

from the molten pool liquid surface is 0.8–1.7 m. Figure 1(a) shows the specific shape and pass layout of the four-hole common oxygen lance nozzle, and Figure 1(b) shows the specific shape and pass layout of the swirl oxygen lance nozzle. The stagnation pressure of both nozzles is 0.84 MPa, and the injection medium is 95%  $O_2$  + 5%  $CO_2$ . In this study, the nozzle throat diameter was  $Dt_1$ , the outlet diameter was  $De_1$ , the included angle between the axis of the oxygen lance nozzle and the axis of the nozzle hole was  $\alpha_1$ , the semi-cone angle of the expansion section was  $\alpha_2$ , and the swirl angle was  $\alpha_3$ .

We used commercial ANSYS Fluent CFD software to produce the simulations in this study. The calculation domain and boundary conditions of the common oxygen lance nozzle are shown in Figure 2(a), showing 627,000 grid points. Figure 2(b) shows the grid and boundary

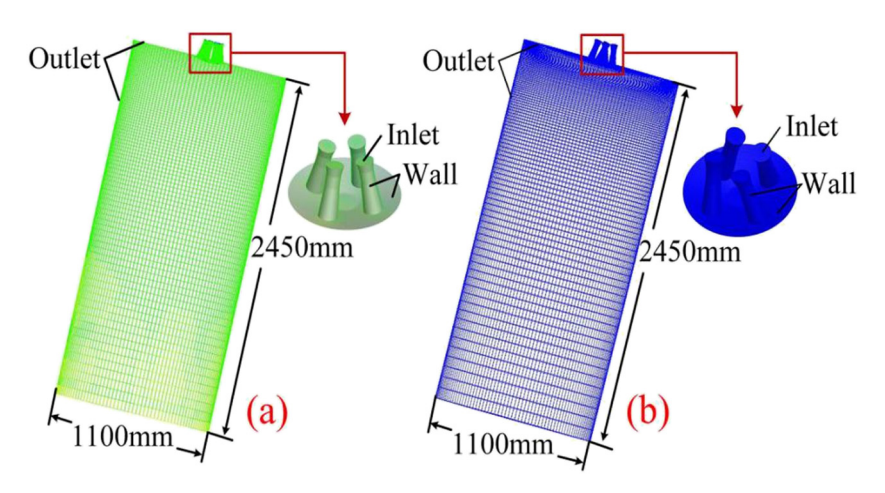


Figure 2: Calculation of the domain and boundary conditions for (a) four-hole common nozzle and (b) four-hole swirling flow nozzle.

condition settings of the four-hole common oxygen lance nozzle with 695,000 grid points. The domain size is 23 times  $De_1$  in the radial dimension and 49 times  $De_1$  in the axial dimension. The inlet boundary is set as a mass flow inlet, the outlet boundary is set as a pressure outlet, and the other boundaries are the wall. The three equations are solved by a density-based coupling solver and discretized by a quadratic upwind scheme [18]. The pressure, velocity, temperature, and density were calculated by an implicit method. Using commercial ANSYS Fluent CFD software, the convergence condition was set to be less than  $10^{-6}$  for the energy term and  $10^{-5}$  for the other terms.

#### 3 Model validation

The axial velocity of a jet hole is measured by a cold jet detection system, and compared with the numerical simulation results to verify the effectiveness of the grid and mathematical model, 24,000 and 27,600 Nm<sup>3</sup>·h<sup>-1</sup> gas flows were used for testing. The cold test system includes a gas source system, injection system, and data analysis system, as shown in Figure 3. The jet cold test system mainly includes a high-pressure gas source, injection system, and data acquisition and processing system; the high-speed and high-pressure gas is ejected from the test nozzle; the jet is converted into a digital signal through the pressure sensor; and the specific velocity value is displayed. After multiple measurements, the velocity field of the test nozzle jet can be completed.

The test results and numerical simulation results of the axial jet velocity of the nozzle are shown in Figure 4. The numerical simulation results are found to be very close to the experimental data for different air supply flows, with a maximum error of 6.3% and an average error of 3.25%. The results in Figure 4 show that the results are in good agreement, which verifies the effectiveness of the model.

#### 4 Results and discussion

In this study, the axial jet characteristics, longitudinal jet characteristics, and average velocity of the jets at different distances between the four-hole common nozzle

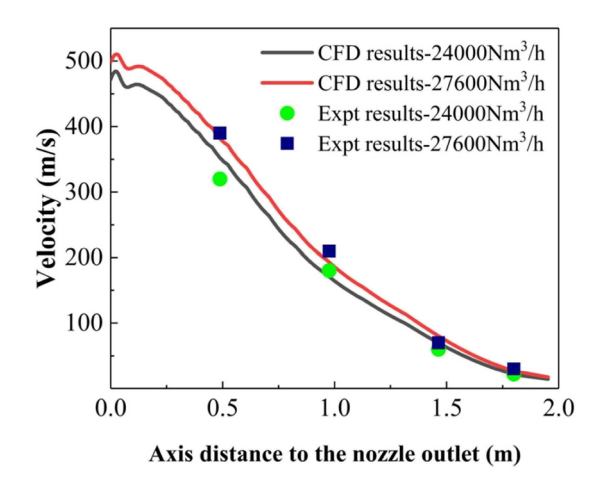


Figure 4: Axial jet velocity distribution of the nozzle orifice.

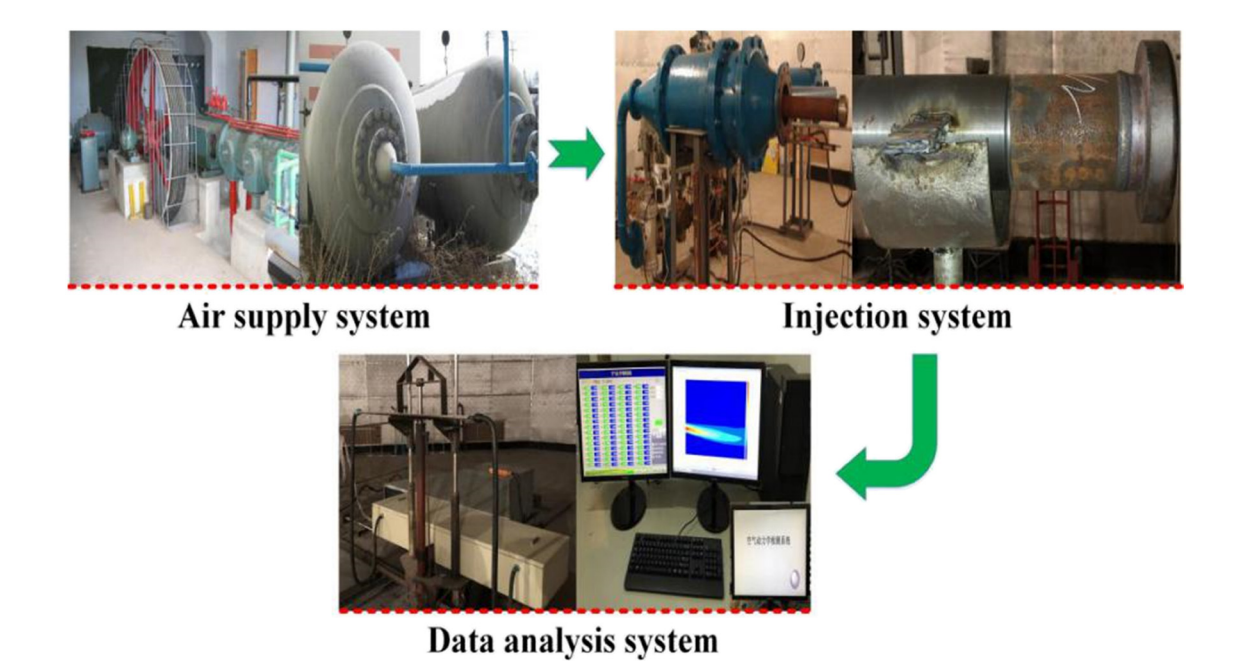


Figure 3: Jet cold test system.

and the four-hole swirl nozzle under different ambient temperatures were analyzed. X is defined as the distance between the designated position and the nozzle, and  $X/De_1$  is set at values of 10 and 20. With these assumptions, the data from the numerical simulation results are obtained, facilitating the analysis of the jet characteristics of the four-hole common nozzle and four-hole swirl nozzle under different temperature conditions.

#### 4.1 Axial distribution of jet characteristics

#### 4.1.1 Jet characteristics of the Laval nozzle axis

The simulation results of the four-hole common and four-hole swirl oxygen lance nozzles were analyzed, and

the jet characteristics under different temperature conditions were obtained. Equations (10)–(13) give a series of equations, such as Mach number and the relationship between temperature and Mach number.

$$Ma = \frac{v}{a} = \frac{v}{\sqrt{ygRT}},$$
 (10)

$$\frac{T}{T_0} = \left(1 + \frac{(\gamma - 1)M^2}{2}\right)^{-1},\tag{11}$$

$$\frac{\rho}{\rho_0} = \left(1 + \frac{(\gamma - 1)M^2}{2}\right)^{-\frac{1}{\gamma - 1}} = \frac{T^{\left(\frac{1}{\gamma - 1}\right)}}{T_0},\tag{12}$$

$$v = \sqrt{2 \times \frac{\gamma g R(T_0 - T)}{\kappa - 1}}.$$
 (13)

According to equation (13), the jet velocity increases with the increase in temperature. Figure 5 shows the

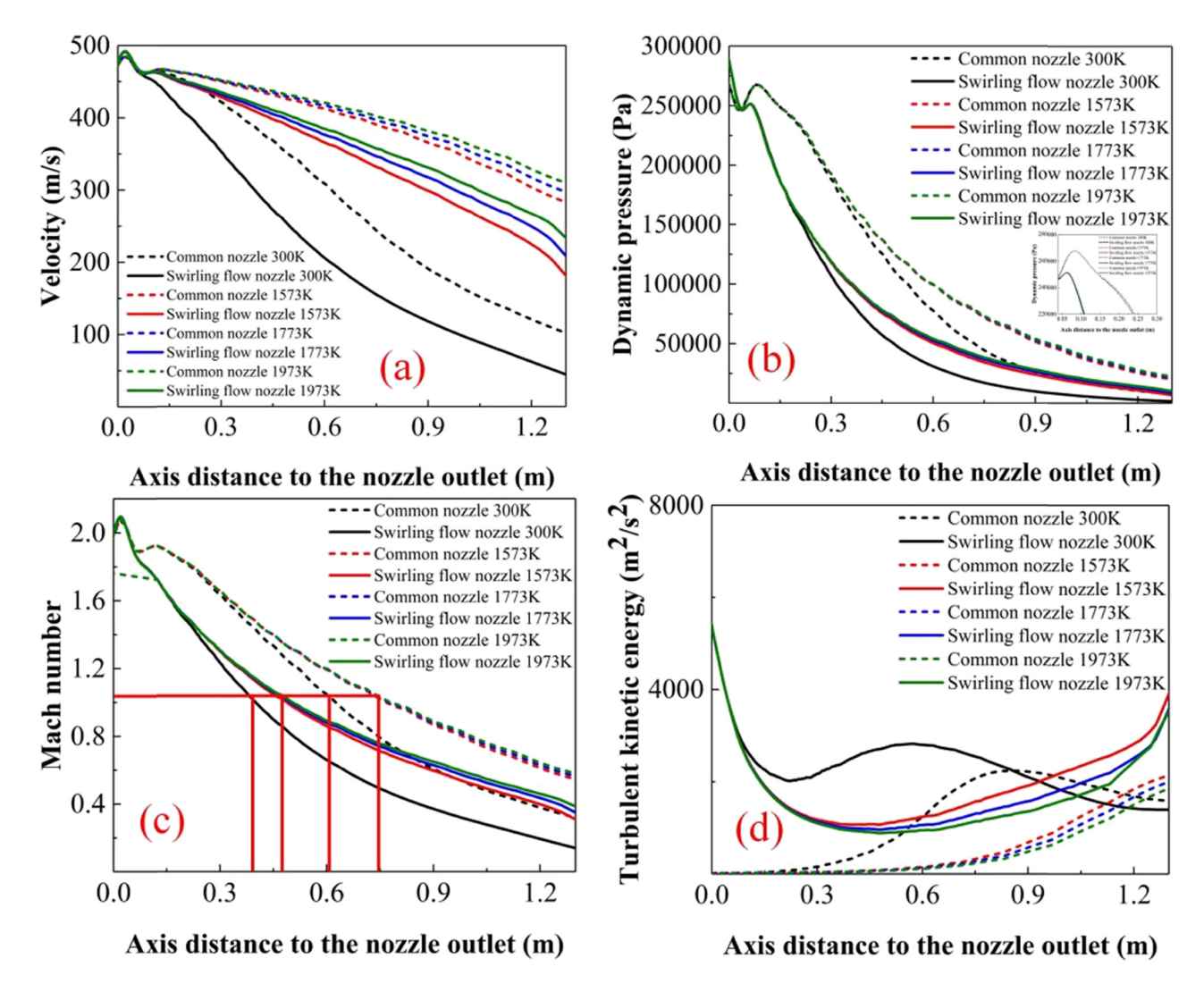


Figure 5: Jet characteristics of the Laval nozzle axis under different temperature conditions. (a) Velocity, (b) dynamic pressure, (c) Mach number, and (d) turbulent kinetic energy.

distribution of jet characteristics at ambient temperatures of 300, 1,573, 1,773, and 1,973 K, respectively. The dotted line represents the common nozzle, whereas the solid line represents the swirl nozzle. Figure 5(a) shows the jet velocity distribution along the Laval nozzle axis under different temperature conditions. It can be seen from the display results that, under the same temperature conditions, the axial velocity of the common nozzle is greater than that of the swirl nozzle. Figure 5(c) shows the change in the Mach number of the Laval nozzle axis. The length of the gas jet with a Mach number greater than 1.0 is defined as the length of the core section. The results show that the length of the core section of the common nozzle is longer than that of the swirl nozzle. The jet distribution along the nozzle axis can be explained as follows. According to the analysis of the jet dynamic

pressure distribution, shown in Equation (12), the gas density decreases with the increase of temperature; the mass of the ambient gas entrained by the jet in the low-density area per unit time is smaller; and the degree of attenuation of the jet velocity is reduced, based on dynamic conservation. It can also be analyzed according to the change results of the jet dynamic pressure in Figure 5(b). The dynamic pressure at the Laval nozzle axis of the common nozzle is higher than that of the swirl nozzle. Therefore, the higher the dynamic pressure, the greater the axial velocity of the jet. Figure 5(d) shows the distribution of the turbulent kinetic energy of the Laval nozzle axis velocity. The results show that the turbulent kinetic energy of the jet hole axis of the swirl oxygen lance nozzle is greater, and the difference in the turbulent kinetic energy is greater at 300 K, which indicates that

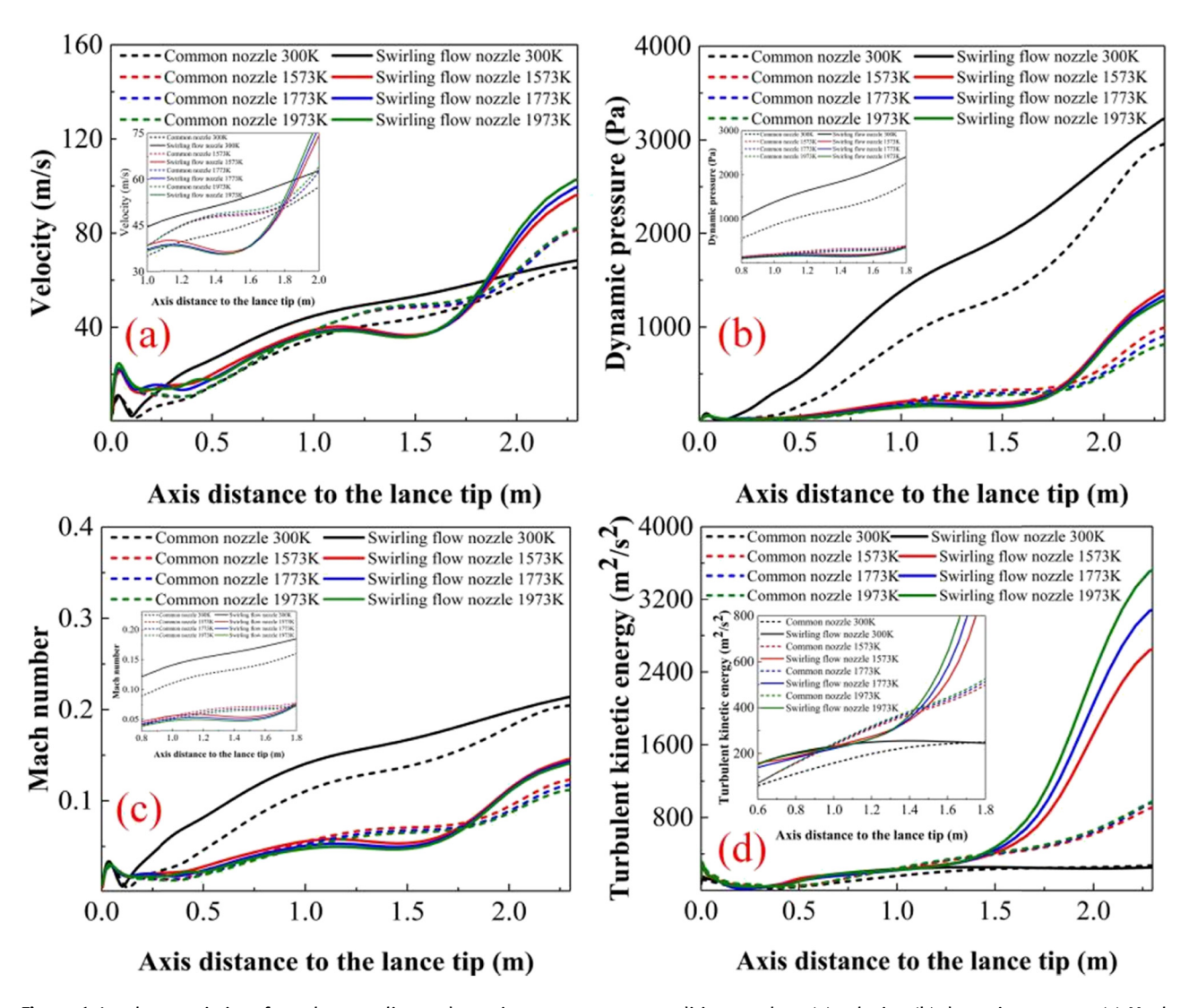


Figure 6: Jet characteristics of nozzle centerline under various temperature conditions such as (a) velocity, (b) dynamic pressure, (c) Mach number, and (d) turbulent kinetic energy.

the jet mixing ahead of time is caused by the deflection angle of 10°, and the radial energy loss of the jet is larger than that of the common nozzle.

## 4.1.2 Jet characteristics of the oxygen lance nozzle centerline

Figure 6 shows the variation in the centerline jet characteristics of the common nozzle and swirl nozzle under different temperature conditions. Figure 6(a) shows the jet velocity distribution along the centerline of the nozzle. The results show that with the increase of distance from the lance tip, the jet velocity increases gradually after 0.12 m away from the nozzle tip, and the centerline velocity and velocity variation of the swirl nozzle are larger

than those of the common nozzle. The centerline velocity of the swirl nozzle at 300 K is larger than that at high temperatures; however, the velocity changes at a slower pace. The centerline velocity distribution results are mainly due to the continuous entrainment of multiple jets in the surrounding gas during the injection process. The increase in centerline velocity of the oxygen lance nozzle is mainly due to the sharp decrease of ambient gas at the centerline, forming a relatively low-pressure area, which offsets the multi-jet flow from the centerline and results in an increase in the centerline velocity. Figure 6(b) shows the flow pressure distribution in the centerline of the nozzle, and Figure 6(c) shows the Mach number distribution of the nozzle centerline. The results show that the dynamic pressure and Mach number of the centerline at 300 K are greater than those at 1,573,

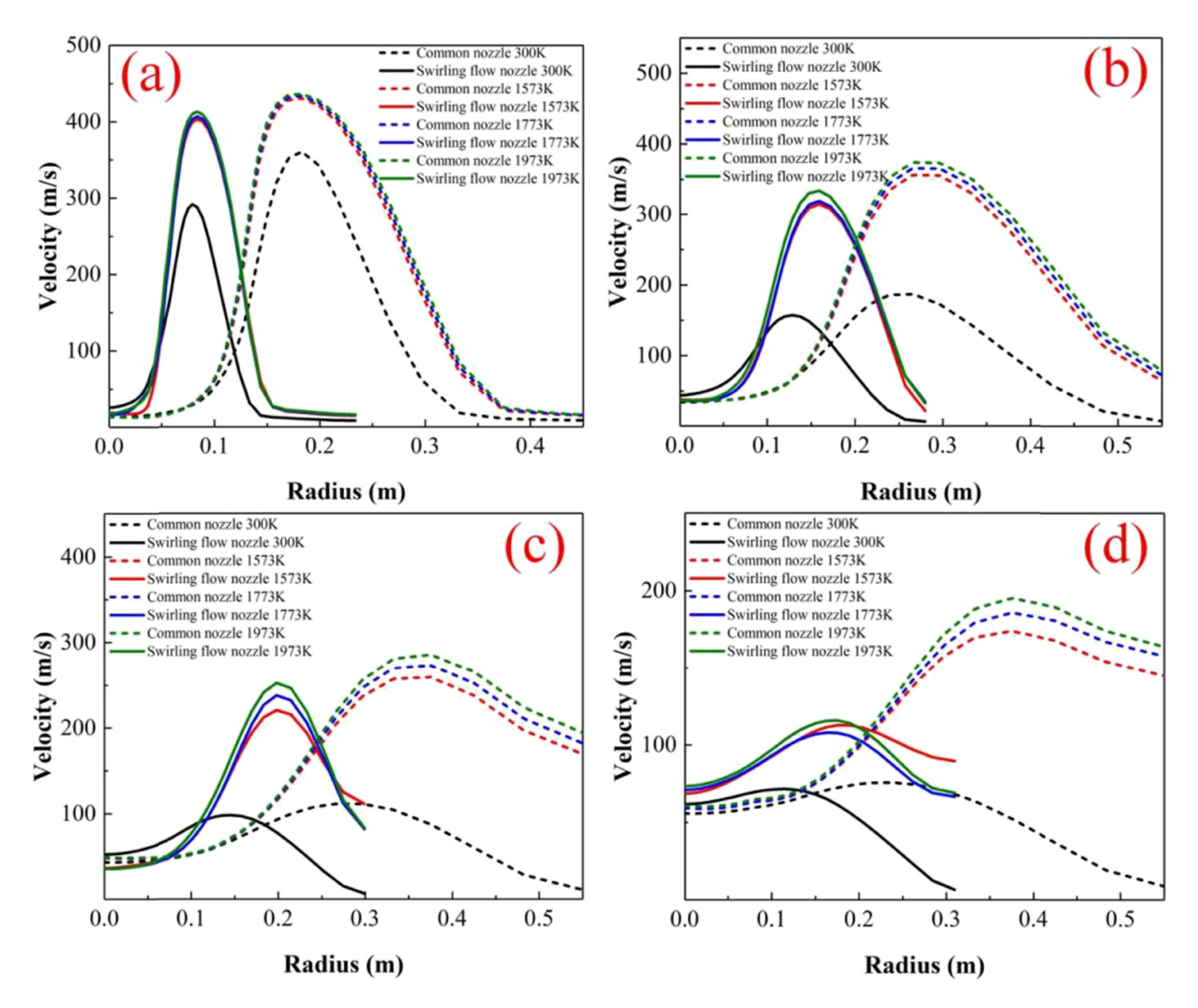


Figure 7: Radial velocity distribution at different temperatures of (a) 10 De1, (b) 20 De1, (c) 30 De1, and (d) 40 De1.

1,773, and 1,973 K, which explains the reason for the larger velocity at 300 K, as shown in Figure 6(a). Figure 6(d) illustrates the distribution of turbulent energy at the centerline. The results show that the turbulent kinetic energy changes very little within 1.25 m from the nozzle; however, the turbulent kinetic energy increases sharply at high temperatures at distances more than 1.25 m, which explains the change in velocity at 1,573, 1,773, and 1,973 K as shown in Figure 6(a). This indicates that the multi-jet mixing of the swirl nozzle is greater than that of the common nozzle beyond a certain distance.

#### 4.2 Radial distribution of jet characteristics

Figure 7 shows the effect of different X/De<sub>1</sub> ratios and ambient temperatures on the radial velocity distribution of the jet. The results show that at the same distance, the maximum velocity point of the common nozzle is farther away from the centerline of the nozzle than the swirl nozzle,

and the velocity itself is higher. The influence of ambient temperature on the jet offset is small; however, higher ambient temperatures correspond to greater maximum jet velocities. With an increase in distance, the maximum value of the jet velocity decreases, and the maximum velocity of the common nozzle is always greater than that of the swirl nozzle. The distribution results can be explained as follows: an increase in X/De<sub>1</sub> leads to a gradual increase in the amount of gas entrained by the jet, and according to the conservation of mass, the jet velocity gradually decreases, which is also consistent with the simulation results in Figure 5(a).

Figure 8 shows the jet velocity field distribution of a common nozzle and a swirling nozzle at temperatures of 300 and 1,973 K. The results show that under the temperature of 300 K, with the increase of distance, the axial velocity of the jet gradually decreases, and the jet center velocity of the common nozzle is higher than that of the swirl nozzle. At 40 De<sub>1</sub>, the multiple jets of the swirling nozzle are seriously mixed and become one jet, which is consistent with the change of maximum radial velocity

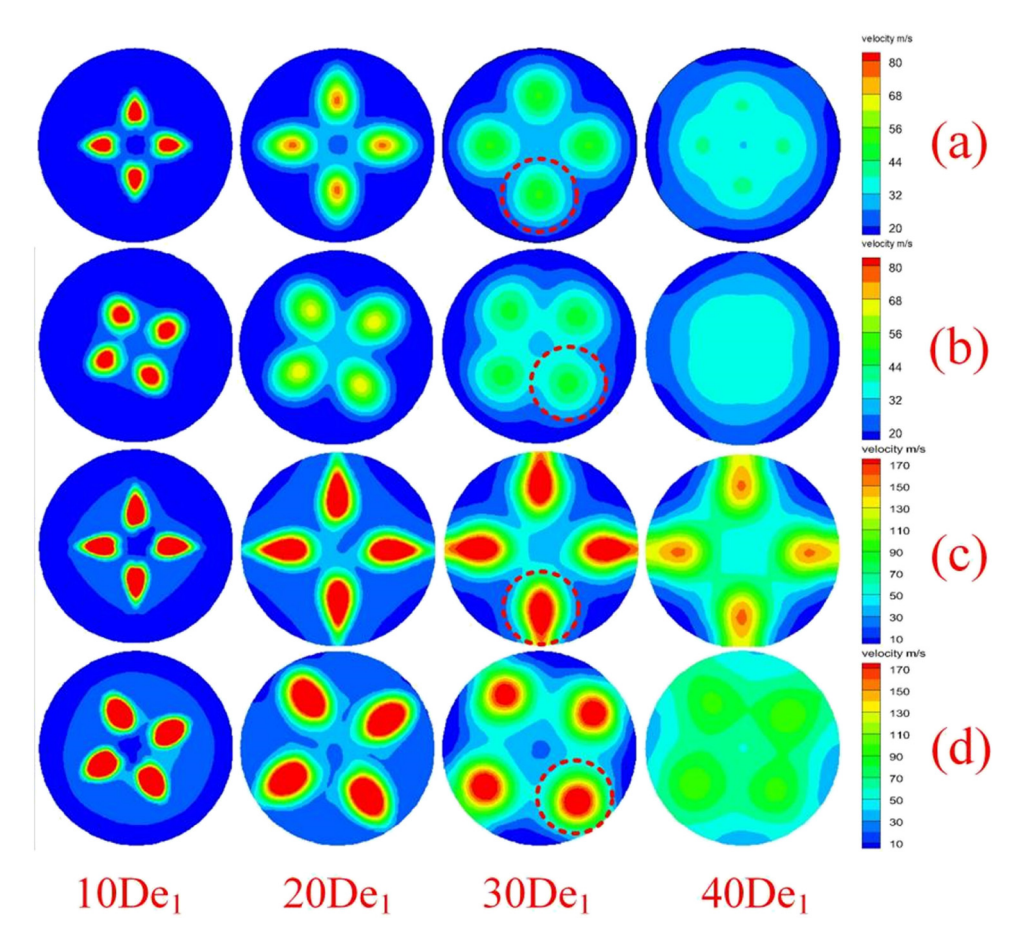


Figure 8: Velocity field at different temperature sections. (a) Ordinary, 300 K; (b) swirling flow, 300 K; (c) ordinary, 1,973 K; and (d) swirling flow, 1,973 K.

shown in Figure 7. At a temperature of 1,973 K, as the distance increases, the axial velocity of the jet gradually decreases, which is a behavior similar to that at 300 K; however, the jet velocity is higher than that at 300 K. At 40De<sub>1</sub>, the maximum jet velocity of the common nozzle is far from the centerline of the nozzle compared with the maximum value of the jet radial velocity and nozzle centerline, as shown in Figure 7. The trend of the change with respect to distance is consistent.

Figure 9 shows the jet radial pressure distribution at different jet distances. The results show that the maximum dynamic pressure of the common nozzle is greater than that of the swirl nozzle, and the maximum jet pressure increases with the increase in ambient temperature at the same distance. The maximum jet dynamic pressure decreases with the increase in injection distance. The results shown in Figure 9 explain the reason for the

variation in the maximum radial velocity of the jet, as shown in Figure 7.

Under the same ambient temperature, the radial distribution of injection velocity under different injection distances is shown in Figure 10. The results show that the maximum jet velocity increases with the increase of ambient temperature, and the velocities at 1,573, 1,773, and 1,973 K are greater than those at 300 K, which is consistent with the velocity distribution results shown in Figure 7. In addition, under the same temperature conditions, with an increase in the injection distance, the distance between the maximum value of the jet center and the centerline of the nozzle gradually increases. However, the increase in the distance between the two types of nozzles does not follow a linear relationship, which is mainly due to the fact that the jets gradually coalesce and the jet centerline shifts to the nozzle axis.

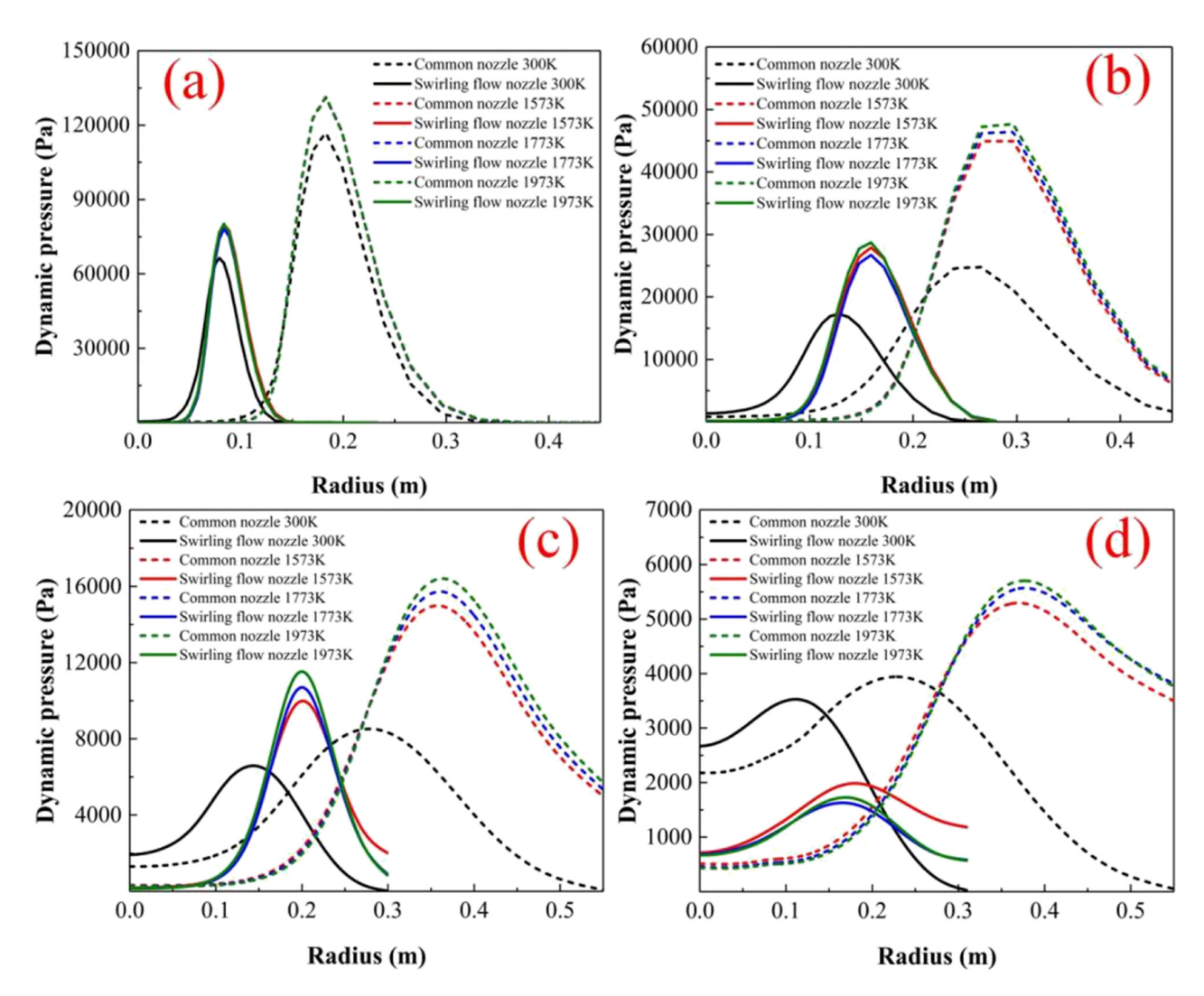


Figure 9: Radial pressure distribution trend of jet. (a) 10 De<sub>1</sub>, (b) 20 De<sub>1</sub>, (c) 30 De<sub>1</sub>, and (d) 40 De<sub>1</sub>.

Compared with the common nozzle, the maximum velocity of the swirl nozzle deviates less from the axis of the nozzle; thus, the jets of the swirl nozzle coalesce earlier.

Figure 11 shows the average cross-sectional velocity changes of the common and swirling nozzles at different temperatures and injection distances. The results show that the increase in ambient temperature is conducive to enhance the mixing ability of the jet to the molten pool. The average jet velocity of the swirl nozzle is higher than that of the common nozzle at X/De<sub>1</sub> of 10 and 20, but lower than that of the common nozzle at X/De<sub>1</sub> of 30 and 40. This is mainly due to the stronger radial mixing force of the swirling nozzle compared with the common nozzle, which can not only realize the impact on the molten pool but also make the molten pool rotate in accordance with the swirl angle direction, producing

a better mixing effect for the molten pool. However, according to the results for  $X/De_1 = 10$ , the multi-jet of the swirling nozzle is more likely to mix. Thus, when the injection distance is large, the jet speed decreases significantly to a value lower than that of the common nozzle.

#### 4.3 Temperature distribution

Figure 12 shows the temperature distribution of the jet axis and nozzle centerline under different ambient temperature conditions. Figure 12(a) shows the temperature distribution of the jet axis for different ambient temperatures. The results show that with an increase in distance, the temperature of the jet axis gradually increases.

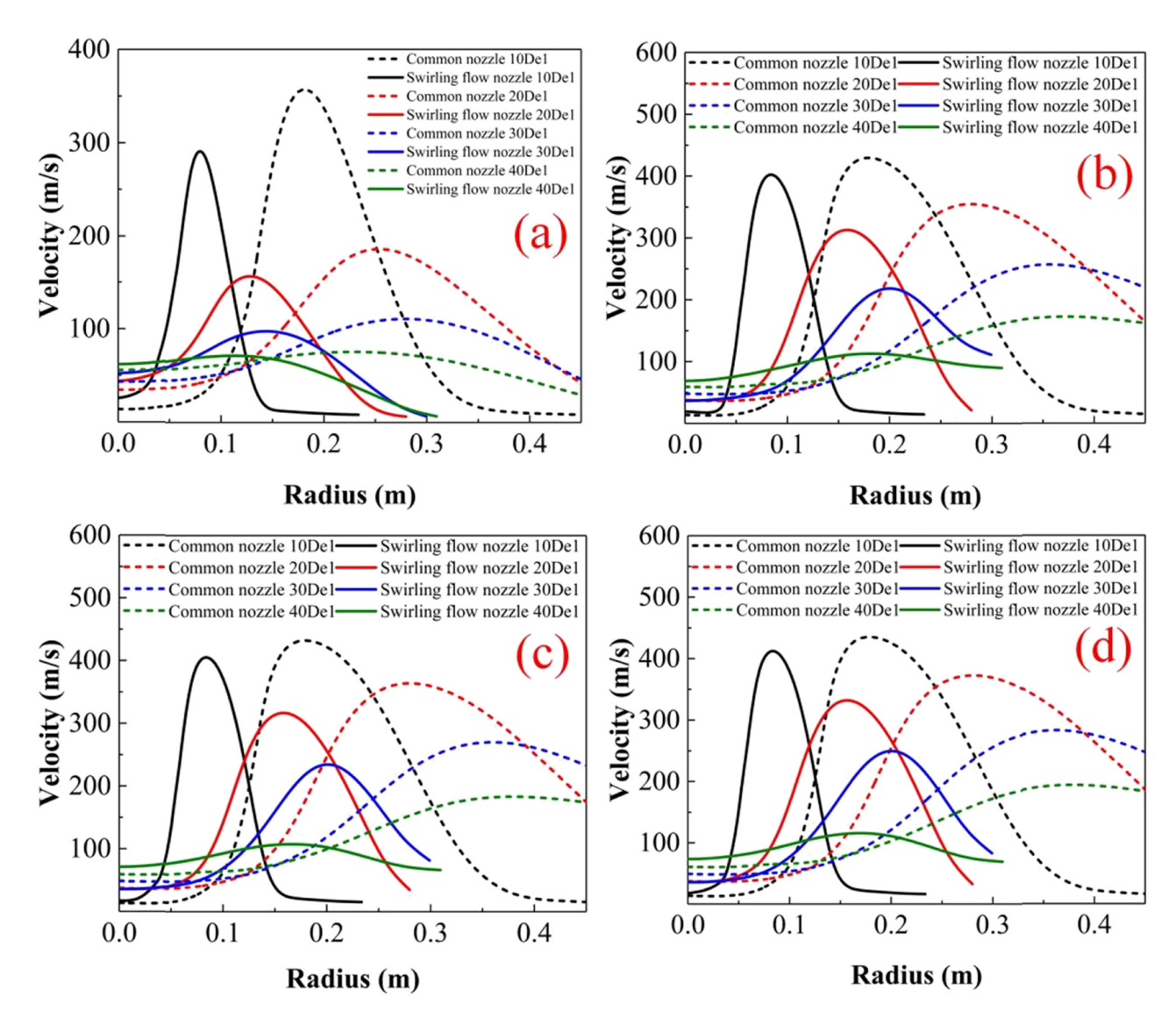


Figure 10: Radial velocity distribution at the same jet velocity with temperatures (a) 300 K, (b) 1,573 K, (c) 1,773 K, and (d) 1,973 K.

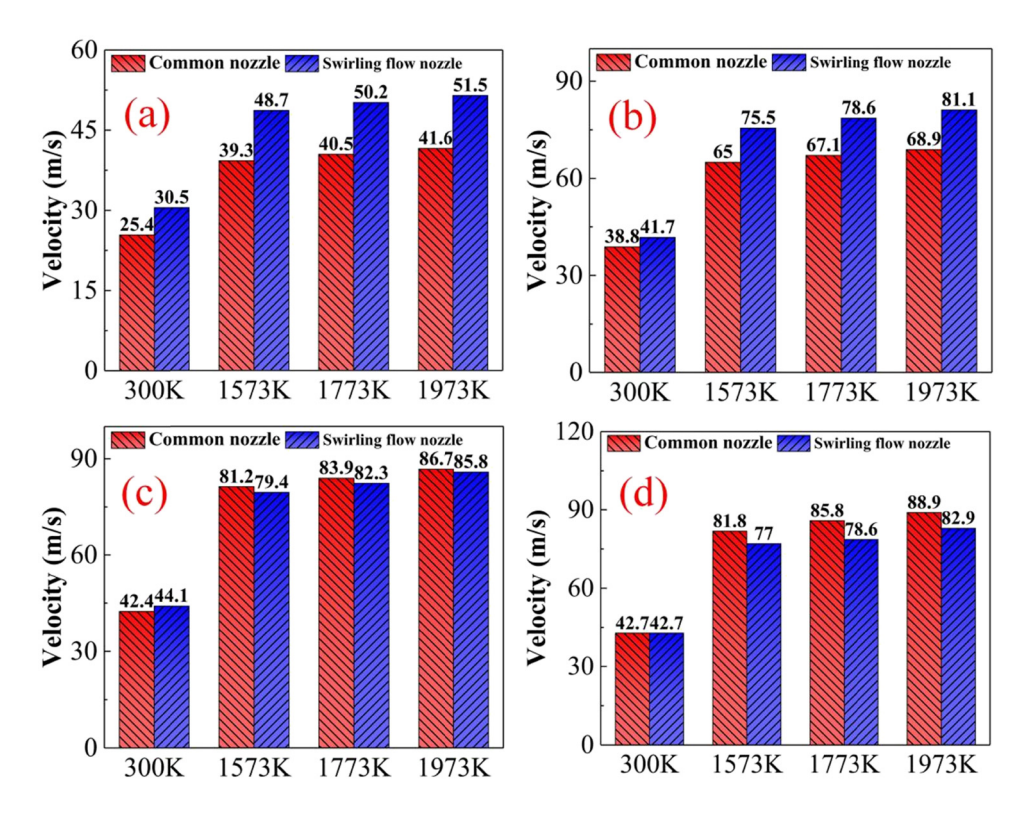


Figure 11: Comparison of cross section velocity values at different temperatures and distances of (a) 300 K, (b) 1,573 K, (c) 1,773 K, and (d) 1,973 K.

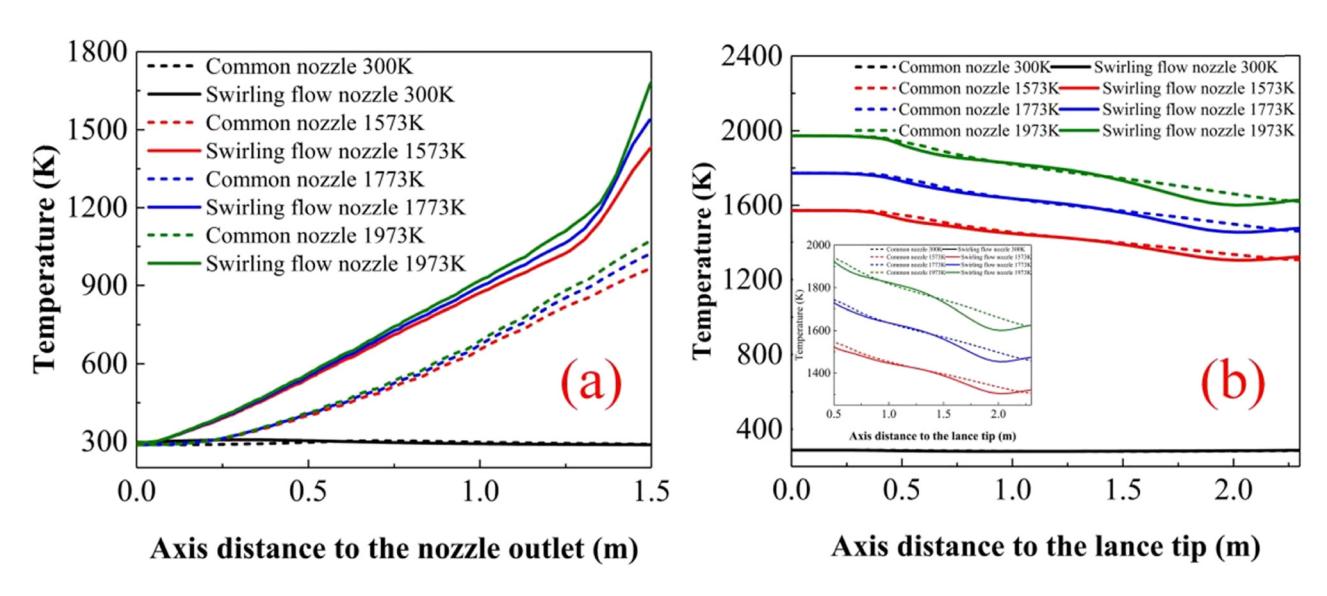


Figure 12: Axial temperature distribution under different ambient temperature conditions. (a) Temperature distribution of jet axis. (b) Axial temperature distribution of oxygen lance nozzle.

Moreover, the axial temperature of the common nozzle is higher than that of the swirl nozzle at the same ambient temperature. The results of the temperature distribution of the jet axis can be explained as follows: the ambient gas is continuously entrained in the jet injection process, and an increase in the ambient temperature inevitably increases the temperature of the jet. With an increase in the injection distance, the amount of ambient gas entrained by the jet increases, resulting in the attenuation of the jet velocity and a gradual increase in the

temperature of the jet axis. According to the conservation of mass, the volume of ambient gas entrained by the common nozzle is less than that of the swirl nozzle; thus, the temperature of the jet axis rises slowly. Figure 12(b) shows the centerline temperature distribution of the nozzle. The results show that with an increase in the distance, the centerline temperature of the nozzle gradually decreases and finally stabilizes. The temperature distribution results from the nozzle centerline can be explained as follows. Because of the multi-jets entraining the ambient gas in the injection process, the gas quantity at the centerline of the nozzle decreases sharply, and the multi-jets coalesce. At the location near the end face of the nozzle, the multi-jets do not deviate, maintaining a good jet state. Therefore, the temperature of the centerline of the nozzle is close to the ambient temperature. The higher the degree,

the higher the centerline temperature. With an increase in the jet distance, multiple jets attract each other and coalesce, and the temperature of the nozzle centerline decreases, owing to the mixing of jets.

Figure 13 shows the radial temperature distribution of the jet at different temperatures. The results show that with an increase in  $\rm X/De_1$ , the radial temperature of the jet gradually increases, the temperature difference between the center point and the radial direction gradually decreases, and the radial temperature curve of the jet exhibits a gentle trend. The minimum value of the radial temperature of the jet of the common nozzle is farther from the centerline of the nozzle than the swirl nozzle. In addition, the minimum radial temperature of the jet increases with the increase in the ambient temperature, and the minimum radial temperature of the common nozzle

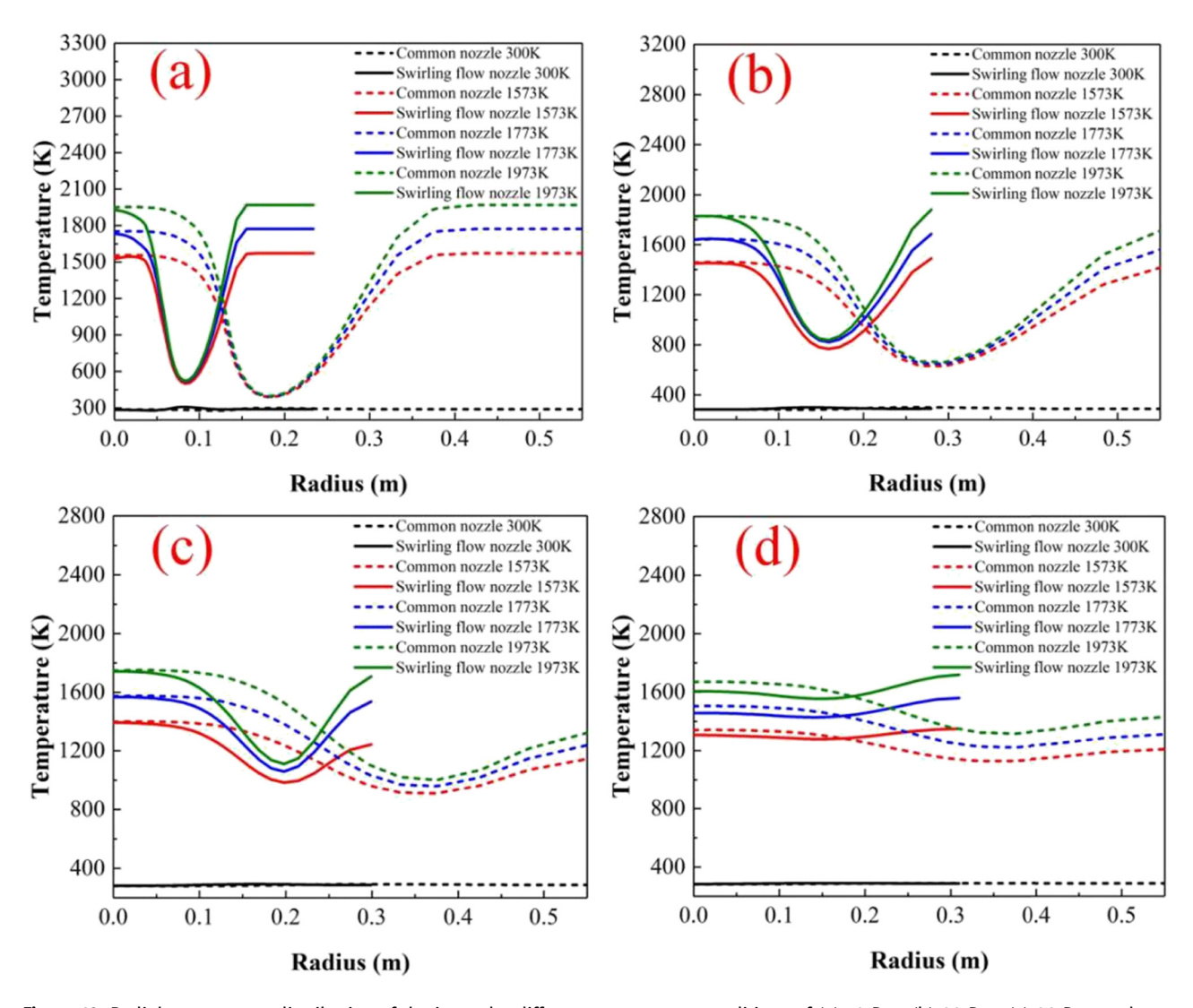


Figure 13: Radial temperature distribution of the jet under different temperature conditions of (a) 10 De<sub>1</sub>, (b) 20 De<sub>1</sub>, (c) 30 De<sub>1</sub>, and (d) 40 De<sub>1</sub>.

is smaller than that of the swirl nozzle. The results of the radial temperature distribution can be explained as follows: with an increase in the jet distance, the temperature difference between the jet center point and the radial temperature gradually decreases, owing to the jet entraining the gas of the surrounding environment. The jet centerline of the swirl nozzle is closer to the centerline of the nozzle than that of the common nozzle; thus, the lowest temperature point of the jet flow is closer to the centerline of the nozzle.

Figure 14 shows the temperature field distribution of the common nozzle and swirl nozzle at 300 and 1,973 K. The results show that the central line temperature and jet axis temperature of the ordinary nozzle are lower than those of the swirl nozzle at the same injection distance. Under the same ambient temperature conditions, with an increase in X/De<sub>1</sub>, the temperature of the centerline area for the common nozzle and swirl nozzle both decrease, and the jet-axis temperature increases. The ambient gas entrained by the jet along the process causes a gradual rise in the temperature of the jet. The temperature at the centerline of the nozzle was found to be higher because

the multi-jets near the nozzle were not mixed; therefore, the temperature in the centerline area of the nozzle decreased, owing to the increase in the degree of mixing.

#### 5 Conclusions

In this study, CFD was used to simulate the jet characteristics of a four-hole common nozzle and a swirl nozzle. The injection medium used was  $CO_2 + O_2$ . The effects of four different ambient temperatures on the jet characteristics of the two types of nozzles were studied. The axial and radial distributions of the jet characteristics under different ambient temperatures; the mixing capacity of jets at different distances; and the distribution of the jet temperature field were discussed. The conclusions of this study are as follows:

(1) The axial jet velocity of the common nozzle and swirl nozzle increases with the increase in ambient temperature, and the jet velocity of the common nozzle is always higher than that of the swirl nozzle. At the

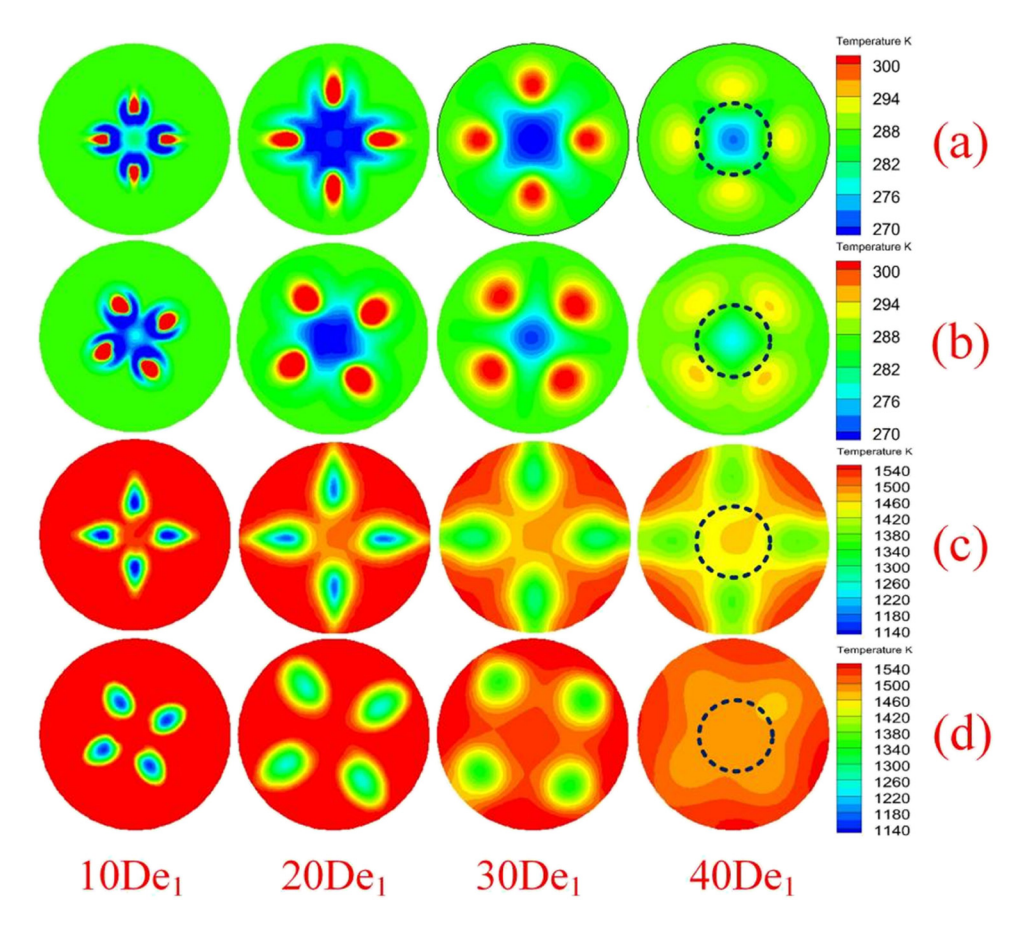


Figure 14: Temperature field distribution under different ambient temperature conditions. (a) Ordinary, 300 K; (b) swirling flow, 300 K; (c) ordinary, 1,973 K; and (d) swirling flow, 1,973 K.

same distance, the maximum velocity point of the common nozzle was farther away from the centerline of the nozzle than the swirl nozzle, and the velocity value was larger.

- (2) An increase in the ambient temperature was found to be beneficial for improving the stirring effect of the jet on the molten pool. The results show that the average jet velocity of the swirl nozzle was higher than that of the common nozzle at X/De<sub>1</sub> of 10 and 20, and that of the swirl nozzle was lower than that of the common nozzle at X/De<sub>1</sub> of 30 and 40.
- (3) With the increase in the ambient temperature and the injection distance, the jet axis temperature of the common nozzle and the swirl nozzle increases, and the nozzle centerline temperature decreases. The jet axis temperature of the common nozzle is always higher than that of the swirl nozzle, while the centerline temperature is always lower than that of the swirl nozzle.

Compared with the common nozzle, the jet of the swirl nozzle has higher radial velocity, enhances the stirring energy near the interface between molten pool and slag, accelerates the dissolution of slag, and is conducive to the interface reaction between slag and metal solution. This kind of nozzle can enhance the metallurgical effect of the dephosphorization converter or vanadium extraction converter. Finally, it should be noted that this study only carried out the analysis and evaluation of the jet characteristics of the common nozzle and swirl nozzle for injecting a 95% O2 and 5% CO2 mixture at different ambient temperatures. Because there are many changing factors in the actual converter smelting production process as well as a series of chemical reactions and combustion reactions that occur, we will make further efforts in the study of this process. This model provides a strong basis for the accurate simulation of the converter smelting process.

**Acknowledgments:** This work was supported by the National Natural Science Foundation of China (Nos. 52004023, NSFC51804028, and 51734003), the Fundamental Research Funds for the Central Universities (FRF-TP-19-031A1), and the China Post Postdoctoral Science Foundation (2019M660459).

**Funding information:** This work was supported by the National Natural Science Foundation of China (Nos. 52004023, NSFC51804028, and 51734003), the Fundamental Research Funds for the Central Universities (FRF-TP-19-031A1), and the China Post Postdoctoral Science Foundation (2019M660459).

**Author contributions:** Chao Feng: Conceptualization, Writing – Original Draft; Kai Dong: Project administration; Rong Zhu: Methodology; Tao Lin: Validation; Jianfeng Dong: Validation; Tao Xia: Supervision; Xin Ren: Investigation.

**Conflict of interest:** Authors state no conflict of interest.

#### References

- [1] Wang, W. J., Z. F. Yuan, H. Matsuura, H. X. Zhao, C. Dai, and F. Tsukihashi. Three-dimensional compressible flow simulation of top-blown multiple jets in converter. *ISIJ International*, Vol. 50, 2010, pp. 491–500.
- [2] Li, Q., M. M. Li, S. B. Kuang, and Z. S. Zou. Numerical simulation of the interaction between supersonic oxygen jets and molten slag-metal bath in steelmaking BOF process. *Metallurgical and Materials Transactions B*, Vol. 46, 2015, pp. 1494–1509.
- [3] Sun, Y. H., X. T. Liang, J. H. Zeng, J. Chen, and L. Chen. Numerical simulation and application of oxygen lance in 120t BOF of PANSTEEL. *Ironmaking & Steelmaking*, Vol. 44, 2016, pp. 76–80.
- [4] Li, L., M. M. Li, L. Shao, Q. Li, and Z. S. Zou. Physical and mathematical modeling of swirling gas jets impinging onto a liquid bath using a novel nozzles-twisted lance. *Steel Research International*, Vol. 10, 2020, pp. 1–7.
- [5] Wei, X. Y., R. Zhu, L. D. Liu, D. S. Zhang, and C. T. Yang. Numerical simulation study on jet-flow of 100t converter oxygen lance. *Steelmaking*, Vol. 27, 2020, pp. 28–30.
- [6] Beketaeva, A., A. H. Abdalla, and Y. Moisseyeva. Investigation of vortex structures for supersonic jet interaction flowfield. *Applied Mechanics and Materials*, Vol. 798, 2015, pp. 5–550.
- [7] Yao, L. J., R. Zhu, Y. X. Tang, G. S. Wei, and K. Dong. Glucosesensing neurons reciprocally regulate insulin and glucagon. *Materials*, Vol. 13, 2020, pp. 2–18.
- [8] Chi, H. L., J. G. Li, and S. Feng. Numerical simulation of death zones in bath under impact of variable angle oxygen lance. *Iron Steel Vanadium Titanium*, Vol. 35, 2014, pp. 91–96.
- [9] Wang, M. L., Y. H. Lv, W. Y. Yang, S. G. Li, and X. W. Xu. Control of equiaxed crystal ratio of high carbon steel billets by circular seam cooling nozzle. *Journal of Iron and Steel Research International*, Vol. 18, 2011, pp. 12–16.
- [10] Garajau, F. S., M. S. Guerra, B. T. Maiaa, P. R. Cetlinb, and D. A. Moreira. Case study: Wear in supersonic nozzle of tip lance in vallourec brazil steelmaking. AISTech 2017 Proceedings: AISTech 2017 Proceedings, Pennsylvania, 2017, pp. 1365–1375.
- [11] Asahara, N., K. I. Naito, I. Kitagawa, M. Matsuo, M. Kumakura, and M. Iwasaki. Fundamental study on interaction between top blown jet and liquid bath. *Steel Research International*, Vol. 82, 2011, pp. 587–594.
- [12] Liu, F., D. Sun, R. Zhu, and J. Ke. Effect of nozzle twisted oxygen lance on flow field and dephosphorisation rate in converter steelmaking process. *Ironmaking & Steelmaking*, Vol. 44, 2016, pp. 640–648.

- [13] Yang, W. Y., C. Feng, M. L. Wang, Y. H. Lv, Y. B. Hu, and X. Y. Peng. Water model experiment of high supplying oxygen blowing in large converter. *Journal of Iron and Steel Research*, Vol. 29, 2017, pp. 807–815.
- [14] Garajau, F. S., M. S. Guerra, B. T. Maiaa, and P. R. Cetlinb. Effects of post combustion temperature on the wear of the supersonic nozzles in BOF lance tip. *Engineering Failure Analysis*, Vol. 96, 2019, pp. 175–185.
- [15] Li, Z. L. and D. Q. Cang. Numerical simulation of supersonic oxygen jets at high ambient temperature. Steel Research International, Vol. 88, 2017, id. 1600209.
- [16] Liu, G. Q., K. Liu, and P. Han. Metallurgical performance of innovative double parameter oxygen lance in BOF steelmaking. *Ironmaking & Steelmaking*, Vol. 27, 2020, pp. 1–10.
- [17] Wei, G. S., R. Zhu, T. Cheng, and F. Zhao. Numerical simulation of jet behavior and impingement characteristics of preheating shrouded supersonic jets. *Journal of Iron and Steel Research*, *International*, Vol. 23, 2016, pp. 997–1006.
- [18] He, C., N. Yang, Q. Huang, L. Wu, Y. Hu, Z. Fu, et al. A multiphase numerical simulation of a four-nozzle oxygen lance top-blown convertor. *Procedia Earth and Planetary Science*, Vol. 2, 2011, pp. 64–69.
- [19] Lv, M., R. Zhu, H. Wang, and R. G. Bai. Simulation and application of swirl-type oxygen lance in vanadium extraction converter. Steel Research International, Vol. 84, 2013, pp. 304–312.
- [20] Li, M. M., Q. Li, Z. S. Zou, and X. Z. An. Integrated application of transcriptomics and metabolomics provides insights into glycogen content regulation in the Pacific oyster Crassostrea gigas. *Metallurgical & Materials Transactions B*, Vol. 48B, 2017, pp. 713–725.
- [21] Yang, L. Z., Z. S. Yang, G. S. Wei, Y. F. Guo, F. Chen, and F. Q. Zhang. Influence of ambient and oxygen temperatures on fluid flow characteristics considering swirl-type supersonic oxygen jets. *ISIJ International*, Vol. 59, 2019, pp. 2272–2282.

- [22] Lv, M., H. Li, X. D. Xing, T. C. Lin, S. Y. Hu, and K. Xie. Variation in multiphase flow characteristics by nozzle-twisted lance blowing in converter steelmaking process. *Steel Research International*, Vol. 93, 2022, id. 202100409.
- [23] Lv, M., H. Li, T. C. Lin, K. Xie, and K. Xue. Behavior of gas-slag-metal emulsion with nozzle-twisted lance in converter steelmaking process. Steel Research International, Vol. 92, 2021, id. 202100103.
- [24] Bi, X. R., R. Zhu, R. Z. Liu, M. Lv, and C. Yi. Fundamental research on CO<sub>2</sub> and O<sub>2</sub> mixed injection stainless steelmaking process. *Steelmaking*, Vol. 28, 2012, pp. 67–70.
- [25] Yin, Z. J., R. Zhu, B. Y. Chen, C. R. Wang, and J. X. Ke. Effect of traditional Chinese medicine Shu-mai-tang on angiogenesis, arteriogenesis and cardiac function in rats with myocardial ischemia. *Iron and Steel*, Vol. 44, 2009, pp. 92-94.
- [26] Zhu, Y. Q., R. Zhu, and X. L. Wang. Thermodynamics analysis of regard CO<sub>2</sub> as RH ascending gas. *Industrial Heating*, Vol. 46, 2017, pp. 7–8,14.
- [27] Lv, M., R. Zhu, X. R. Bi, N. Wei, C. R. Wang, and J. X. Ke. Basic research on control of converter dephosphorization by COMI steelmaking process. *Iron and Steel*, Vol. vol.46, 2011, pp. 36–40.
- [28] Zhang, B. L., R. Zhu, X. L. Wang, J. M. Bian, and L. Luo. Experimental study on 300t converter CO<sub>2</sub>-O<sub>2</sub>: Mixed blowing steelmaking. World Metals, Vol. B03, 2018, pp. 1–4.
- [29] Han, B. C., G. S. Wei, R. Zhu, W. H. Wu, J. J. Jiang, C. Feng, et al. Utilization of carbon dioxide injection in BOF-RH steelmaking process. *Journal of CO<sub>2</sub> Utilization*, Vol. 34, 2019, pp. 53-62.
- [30] Feng, C., R. Zhu, B. C. Han, L. J. Yao, W. H. Wu, G. S. Wei, et al. Effect of nozzle exit wear on the fluid flow characteristics of supersonic oxygen lance. *Metallurgical and Materials Transactions B*, Vol. 51, 2020, pp. 187–199.